Experimental determination of a species-dependent effect in the transverse emittances of sputter-generated negative-ion beams

G. D. Alton and R. W. Sayer
Oak Ridge National Laboratory, Post Office Box 2008, Oak Ridge, Tennessee 37831-6368
(Received 16 January 1989)

We report experimental evidence of a previously unseen species-dependent effect in the transverse emittances of momentum-analyzed $^{28}Si^-$, $^{58}Ni^-$, and $^{197}Au^-$ negative-ion beams generated by cesium-ion sputtering. The differences in the emittances are found to be principally correlated with differences in the energy spreads in the respective ion beams, which have their origins in the sputter-ejection negative-ion formation process. The experimental equipment and techniques utilized for emittance data acquisition and analysis, and evidence for a species-dependent effect in the emittances and brightnesses of the subject ion beams, are presented in this paper.

I. INTRODUCTION

In recent years, the sputter process, in combination with the work-function-lowering aspects of group IA elements, has been utilized as a versatile, relatively efficient, and practical means of producing negative ions. This technique is widely utilized for producing a variety of atomic and molecular negative-ion beams for use in accelerator-based atomic, nuclear, and applied research programs, as well as the important analytical fields of secondary-ion mass spectrometry (SIMS) and tandem mass spectroscopy (TMS). Several negative-ion sources predicated on this principle have been described in the literature.[1-3]

Although progress has been made towards a better understanding of the negative-ion generation process, the precise mechanism is still the subject of varying opinions.[4-8] Blaise and Nourtier[9] and Williams[10] have reviewed the subject of ion emission from clean metal and chemically complex surfaces, respectively, while a more general review has been given by Wittmaack.[11] Vasile[12] has included discussions of the principal models that have been proposed for description of these phenomena. The reader is referred to these articles and others in the literature for more detailed expositions on the subject.

The key physics question associated with all of the proposed theoretical models is the role that the velocity dependence plays in the secondary-ion formation process. In models based upon local thermodynamic equilibrium in the region of primary ion impact with the surface, secondary-ion emission depends weakly on ion emission velocity.[7,8] On the other hand, models that involve atomic excitation followed by electron capture or loss by the atom or molecule as it leaves the surface predict a much stronger velocity dependence for secondary-ion emission.[4-6]

Time-dependent perturbation quantum-mechanical treatments of the problem have been made by Blandin, Nourtier, and Hone[4] and Nørskov and Lundqvist,[6] which describe the electron attachment or loss probabilities as the atom moves across the surface boundary. Nørskov and Lundqvist[6] used this theoretical basis to arrive at expressions for the probabilities for positive and negative-ion emission, $P^+(v_\perp)$ and $P^-(v_\perp)$. Experimental evidence in support of a velocity-dependent mechanism has been presented by Vasile for positive-ion formation[12] and by Yu for negative-ion formation.[13] In this paper, we are only interested in $P^-(v_\perp)$.

In an earlier work, Yu established a direct correlation between the value of the work function during cesium adsorption and the yield of Mo^- produced by Ne^+ sputtering of clean Mo surfaces.[5] The secondary negative-ion emission probabilities were observed to increase rapidly with decreasing surface work function and to reach maxima whenever the work function reached its minimum value. These results strongly support a surface ionization mechanism for secondary negative-ion formation.

The probabilities for negative-ion formation in the Nørskov and Lundqvist prescription can be cast into a simple energy-dependent form given by

$$P^-(E_2,\theta) = \frac{2}{\pi}\exp\{-\beta\sqrt{M_2}[\phi(\sigma)-E_A+V_i]/\sqrt{2E_2}\cos\theta\}\ , \tag{1}$$

where M_2 is the mass of the ion of energy E_2 with electron affinity E_A, V_i is the image potential induced in the surface by the escaping ion, θ is the polar angle with respect to the surface normal, and β is a constant. The work function ϕ depends on the relative adsorbate surface coverage σ. Equation (1), in fact, must be integrated over a properly normalized sputtered particle energy-angular distribution function $f(E_2,\theta)$ to determine the total probability for negative-ion formation. Of specific interest are the negative-ion yields or ion currents achievable in ion sources predicated on this principle. If we ignore destructive effects due to high positive-ion current densities and interference to sputtering by adsorbate atoms at high surface coverages, we can express the ion current I^- as follows:

$$I^- = 4I^+(E_1)S(E_1,\theta_i)\int_{V_i}^{E'}\int_0^{\pi/2} f(E_2,\theta)\exp\{-\beta\sqrt{M_2}[\phi(\sigma)-E_A+V_i]/\sqrt{2E_2}\cos\theta\}\sin\theta\, d\theta\, dE_2 \quad (2)$$

In Eq. (2), I^+ is the positive-ion current and $S(E_1,\theta_i)$ is the sputter ratio of the target at projectile energy E_1 at an angle of incidence with respect to the surface normal θ_i. In Eq. (2), the limits of integration over E_2 are taken between V_i and E' where E' is the maximum energy transfer possible in the first collision between a projectile of energy E_1 and mass M_1 and an atom in the solid of mass M_2. In this case, E' is given by the relation

$$E' = 4M_1M_2E_1/(M_1+M_2)^2 .$$

Hence, the energy distributions of negative neutral particles depend on the energy E_1 and mass M_1 of the projectile. Experimental measurements of the energy distributions of neutral sputter particles[14] are in support of the Sigmund-Thompson distribution[15,16] given by

$$f(E_2,\theta) = A_N\frac{E_2}{(E_2+E_b)^3}\cos\theta , \quad (3)$$

where E_b is the surface binding energy of the particle in the solid, E_2 the energy of the ejected particle, and A_N is a normalization constant determined by requiring the integral of Eq. (3) over all energy and angles be equal to unity. Energy distributions of a few sputter-generated negative-ion beams produced by cesium-ion sputtering have been reported by Doucas.[17]

Assuming the appropriateness of Eqs. (2) and (3) for the description of the secondary-ionization process, we can readily see the importance that the energy E_2 plays in determining the probability for negative-ion formation and, consequently, the total negative-ion yield from ion sources predicted on this principle. Since the image potential V_i is of the order of 1.5 V, the particle ejection energy E_2 must be equal to or greater than this value. It is known from experimental measurements that the full width half maxima (FWHM's) of negative-ion[17] and neutral[14,18] sputtered particle energy distributions vary from element to element. Observed differences in energy spreads would exhibit themselves as differences in the emittances of the respective ion beams brought about by chromatic aberration of the beam by lenses, and dispersive devices (magnets) in transit to the emittance measurement apparatus. Thus, based on these arguments, the emittances of ion beams of different species should reflect a species-dependent effect. However, no such effect has been reported.

During previous investigations,[19,20] attempts were made to delineate intensity and species-dependent effects from the emittances of ion beams extracted from a number of negative-ion sources based on the sputter principle, including the ellipsoidal geometry ionizer source[20] used in the present investigations. From these data, a moderate intensity-dependent effect was observed, which was subsequently attributed to changes in the positive-ion beam size at impact with the surface due to optical effects associated with changes in the probe voltages used to increase the beam intensity and not to space-charge effects within the negative-ion beams.

From these earlier investigations,[19,20] it was also noted that the emittances of Si^- negative-ion beams were consistently 15–20 % lower than ion beams such as Ni^- and Au^-. This finding was more pronounced for ionizer geometries which sharply focused the cesium-ion beam onto the sample surface. However, this effect was not clearly delineated in these early experiments. This observation prompted us in the present effort to look more carefully for the effect with the ellipsoidal geometry source, which focuses the cesium-ion beam to a well-defined region of the sample surface.

II. DEFINITIONS

A. Liouville's theorem

Liouville's theorem states that the motion of a group of particles under the action of conservative force fields is such that the local number density in the six-dimensional phase-space volume (hypervolume) $xyzp_xp_yp_z$ everywhere remains constant. The theorem applies to an ion beam subjected to conservative force fields. The quality of an ion beam is usually expressed in terms of emittance ϵ and brightness B. Both are related to Liouville's theorem.

B. Emittance

For ion beam transport, the components of phase space transverse to the direction of beam motion are usually the most important. If the transverse components of motion of a group of particles are independent in configuration space, the motion of the particles in the orthogonal planes (x,p_x), (y,p_y), and (z,p_z) will be uncoupled and, therefore, the phase spaces associated with each of these planes will be separately conserved. These conserved areas of phase space in the respective directions of motion are referred to the emittance ϵ of the ion beam.

The conserved components of transverse phase space are taken to be elliptical in shape, the areas of which are given by

$$A_x = \pi x p_x, \quad A_y = \pi y p_y . \quad (4)$$

For the case where the component of momentum along the z direction of the beam p_z is approximately constant

$$\begin{aligned} A_x &= \pi x p_z \tan\theta_{xz} = \pi x M_2 \tan\theta_{xz}\beta\gamma c , \\ A_y &= \pi y p_z = \pi y M_2 \tan\theta_{yz}\beta\gamma c , \end{aligned} \quad (5)$$

where $\beta = v/c$ and $\gamma = 1/[1-(v/c)^2]^{1/2}$. In expressions (5), M_2 is the mass of the particle of velocity v, c is the velocity of light, and θ_{xz}, θ_{yz} are the angles that the transverse components of the particle's motion make with the component of motion along the z axis. In the small-angle approximation,

$$\tan\theta_{xz} \approx \theta_{xz} = \frac{dx}{dz} = x' \tag{6}$$

and

$$\tan\theta_{yz} \approx \theta_{yz} = \frac{dy}{dz} = y' \tag{7}$$

so that

$$A_x \approx \pi x x' M_2 \beta\gamma c \quad \text{and} \quad A_y \approx \pi y y' M_2 \beta\gamma_c \ . \tag{8}$$

For the nonrelativistic case,

$$A_x \approx \pi x x' \sqrt{2M_2 E} \quad \text{and} \quad A_y \approx \pi y y' \sqrt{2M_2 E} \ , \tag{9}$$

where E is the energy of the ion beam. The emittance ϵ of the ion beams is proportional to the transverse phase space and thus is also a conserved quantity. The following energy E and velocity v dependent definitions have been adopted historically for the definitions of normalized emittance ϵ_{nx} and ϵ_{ny}:

$$\epsilon_{nx} \approx \pi \left| \int\int \frac{dx\, dx'}{\pi} \right| \sqrt{E}$$

and (10)

$$\epsilon_{ny} \approx \pi \left| \int\int \frac{dy\, dy'}{\pi} \right| \sqrt{E}$$

or

$$\epsilon_{nx} \approx \pi \left| \int\int \frac{dx\, dx'}{\pi} \right| \beta\gamma$$

and (11)

$$\epsilon_{ny} \approx \pi \left| \int\int \frac{dy\, dy'}{\pi} \right| \beta\gamma \ ,$$

where the integrations are performed over the emittance contour that contains a specified fraction of the beam (e.g., 10%, 20%, etc.). In this study Eq. (10) was utilized as our definition for emittance.

C. Brightness

Another figure of merit often used for evaluating ion beams is the brightness B. Brightness is defined in terms of the ion current dI^2 per unit area dS per unit solid angle $d\Omega$ or

$$B = \frac{dI^2}{dS\, d\Omega} \ . \tag{12}$$

In terms of normalized brightness, Eq. (12) can be shown to be equivalent to[21]

$$B_n = \frac{2dI^2}{\epsilon_{nx}\epsilon_{ny}} \ . \tag{13}$$

For purposes of convenience, we define brightness as

$$B_n = \frac{2dI^2}{\epsilon_n^2} \ , \tag{14}$$

where

$$\epsilon_n = \sqrt{\epsilon_{nx}\epsilon_{ny}} \ . \tag{15}$$

III. EXPERIMENTAL EQUIPMENT, DATA ANALYSIS, AND EXPERIMENTAL PROCEDURES

A. Source description

The source utilized in these experiments is equipped with a solid tungsten ellipsoidal geometry ionizer for producing positive cesium-ion beams, which, in turn, are used to sputter a negatively biased probe containing the material of interest. A more detailed description of this source, along with the emittances of ion beams extracted from the source, has been given previously.[20,22] In such sources, the material of interest is mounted on a negatively biased probe that is typically maintained at potentials of 1–5 kV with respect to the housing in a controlled vapor flux of a group IA element, usually cesium. Cesium is most commonly used because it has the lowest first ionization potential of the group IA elements (3.89 eV): as an adsorbate, cesium also effects the greatest changes in work function[23] and thus is the most effective of the group IA elements in forming negative ions through surface ionization processes. Ions, ionized by direct surface ionization from a hot surface or by electron impact plasma discharge ionization, are accelerated to the negatively biased probe where they sputter the sample of interest. Negative ions are then formed by secondary surface ionization processes and extracted from the source. The source used in these experiments is shown schematically in Fig. 1. Cesium-ion trajectories resulting from computer simulation studies are superimposed to illustrate the strong focusing characteristics of this source geometry. The size and shape of the observed wear patterns for these sources, as well as those computationally predicted, are sensitive to sample position because of the strongly convergent nature of the cesium-ion beam. For standard source operation, the sample is always placed at the focal point of the positive cesium-ion beam; the positive-ion current density distribution on the sample surface determines the region of negative-ion generation, which, in conjunction with the aperture size, the aperture distance from the sample surface, and characteristics of the sputter process, essentially determines the emittances of extracted ion beams. The negative-ion extraction aperture (4.5-mm diameter) limits the negative-ion beam to a half angle of 5.8° at the exit. Initially, all negative-ion beams leave the source with the same maximum angular divergence, irrespective of ion species.

B. The ion source test facility

Emittance measurements of the ion beams extracted from the ellipsoidal geometry ionizer source were made by use of the equipment and procedures described in this section. The source and einzel lens were mounted on an ion source test facility, shown schematically in Fig. 2. With this facility, negative-ion beams with energies up to 30 keV may be produced. However, 20 keV was typical

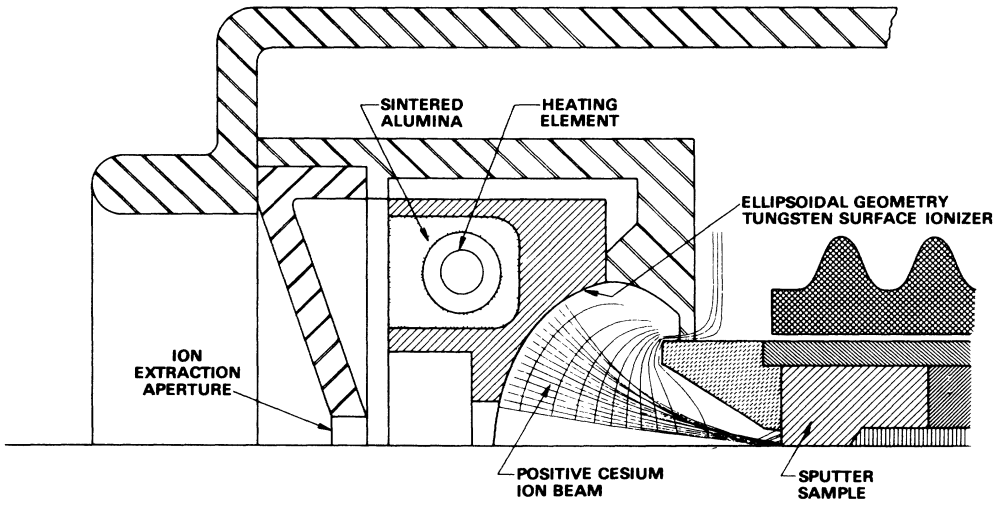

FIG. 1. Schematic drawing of the ellipsoidal geometry ionizer negative-ion source showing computer simulated cesium-ion trajectories in the ionizer-sputter probe region of the source.

of these present measurements. In addition to the ion source and beam transport lens, the facility consists of a double-focusing magnet, the emittance measuring device, beam line component valves, turbomolecular pumping stations, and auxiliary power supplies required for system operation. Negative-ion beams are extracted from the source at an energy of 3 keV, postaccelerated to a final energy of 20 keV, and focused by means of the einzel lens onto the object plane of the magnet. Ions of the desired mass are then deflected through 90° and focused at the image position of the system. The intensity of the negative-ion beam can be monitored prior to and following momentum analysis by insertion of remotely actuatable Faraday cups; the Faraday cups are located immediately behind variable slit-type apertures, which are positioned at the object and image planes of the momentum analysis system. With the Faraday cups removed, the beam passes onto the slit detector unit of the emittance measurement device where determinations are made of the emittance of a particular ion beam.

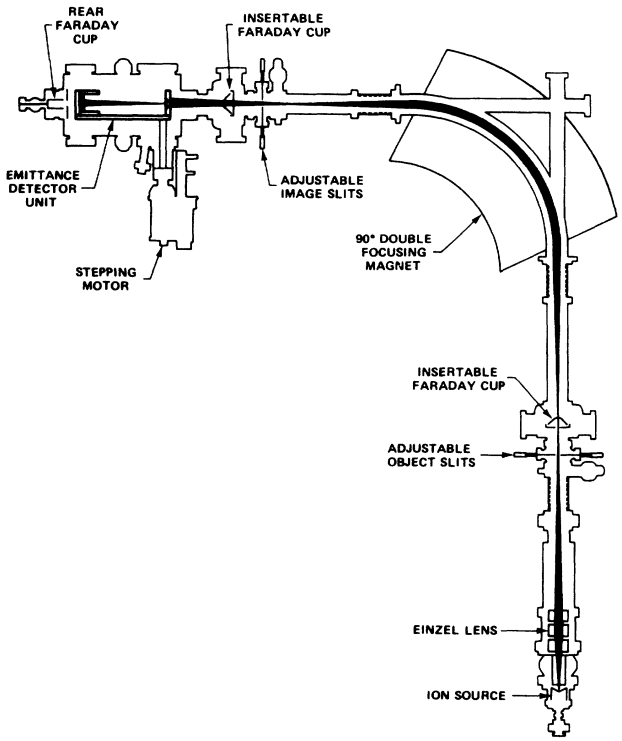

FIG. 2. Schematic drawing of the ion source test facility.

C. The emittance measuring apparatus

The emittance measurement device has been described in detail previously[19,20,22] and, therefore, only a brief reiteration will be given here. The device consists of a vacuum housing, two identical stepping motor driven detector units for determining the emittances of an ion beam in either the x or y direction, and a control unit for driving the detector hardware. The control unit consists of a microcomputer that is interfaced to a CAMAC crate controller, an input-output register, a stepping motor controller, and a 12-bit analog-to-digital converter (ADC). The CAMAC crate control modules communicate with the emittance measurement hardware via an external electronics unit.

The ion beam diagnostic unit consists of an electrically isolated slit aperture (width: 0.1 mm, length: 50 mm), positioned 0.4 m in front of a detector unit (angular resolution: 1 mrad) that is made up of 32 electrically isolated plates. The current striking each of the detectors is used to determine the differential angular divergence of the ion beamlet which is allowed to pass through the slit aperture at a given x or y position. An emittance measurement

consists of stepping the slit detector system through an ion beam in a chosen direction while monitoring the total ion current striking the slit unit and the differential ion currents striking each of the 32 detectors at each of 50 positions during a selectable integration time period. The signals are integrated, digitized, and stored in memory of the microcomputer for later data analysis.

D. Data analysis

Equi-intensity contour levels which contain 10–80% of the total beam are calculated iteratively in increments of 10% to an accuracy of 0.1% and are determined by performing a Simpson's rule volume integration over the xx' or yy' versus intensity data set. The contour level information is then passed to a topographical graphics program that produces contour plots from the data. The area within a particular contour is the emittance for this particular beam fraction.

IV. EXPERIMENTAL PROCEDURES

Throughout the course of the investigations, the ion source operational parameters of cesium oven temperature (196 °C), sputter probe voltage with respect to housing (−3 kV), ion extraction voltage (−20 kV), and sample position with respect to the cesium surface ionizer were maintained at precisely the same settings for each of the samples. Prior to emittance data accumulation, the ion beams were allowed to stabilize, typically, for a few hours. Negative-ion beams formed by 3-keV cesium-ion beam bombardment of the samples were extracted from the source, further accelerated to a final energy of 20 keV, and subsequently transported through the ion source test facility discussed previously. The einzel lens was used to focus the ion beams onto the object point of the double-focusing magnet. Beam intensities were monitored prior to and following momentum analysis to assure source alignment and total beam transport to the emittance-measuring device. Emittance measurements were then made utilizing the hardware procedures and data analysis techniques described previously.

V. CONTRIBUTIONS TO EMITTANCE GROWTH

Active ion optical elements can increase the phase space of an ion beam through three dominant types of aberrations: geometrical, chromatic, and parasitic or mechanical. Geometrical aberrations arise from third-order contributions to the image size; chromatic aberrations reflect the fact that lenses are strongly dependent on the energy, angular divergence, and energy spread of the ion beam; parasitic aberrations arise because of imperfect mechanical alignment. Of the several classifications of geometrical aberrations, spherical aberrational effects are of principal concern in this ion beam transport system. The control of parasitic aberrations is well understood and is assumed to be negligible in this experimental arrangement. Space charge effects after extraction from the source are also considered negligible at the beam intensities involved in this experiment.

A. Lens aberrations

1. Spherical aberration

An object imaged by a lens system will be increased by an amount Δr_i given by[24]

$$\Delta r_i = MC_{so}\theta_o^3 , \tag{16}$$

where M is the magnification, C_{so} is the coefficient of spherical aberration referred to in the object side of the lens, and θ_o is the half angle of arrival at the lens. The spherical aberration coefficient depends on the focal length of the lens and is lens specific. The image grows directly with the coefficient and, therefore, a low value is desired. For a given spherical aberration coefficient, image growth can be controlled by limiting θ_o.

Spherical aberration coefficients have been measured for an einzel lens very close to the lens used in these experiments.[25] We shall, therefore, use these data to determine the coefficient of spherical aberration C_{so} and subsequently beam size growth due to spherical aberration by the einzel lens.

2. Chromatic aberration

The einzel lens potential difference and ion energy occur in the expression for the focal length of an electrostatic lens. Distortion will occur in the image due to (1) changes in the accelerating potential during ion transit through the lens, (2) energy spread in the ion beam, (3) inelastic collisions between the ion and solid or gas scatterers, and (4) large angular divergence in the ion beam.

For the case of chromatic aberrations, an object imaged by a lens system will be increased in size by an amount[24]

$$\Delta r_i = MC_{co}\theta_o \frac{\Delta E}{E} , \tag{17}$$

where M is the magnification, C_{co} is the coefficient of chromatic aberration referred to the object plane, θ_o is the angle of departure from the object position, ΔE is the energy spread of the beam of mean energy E at the object side of the lens. From this expression, we see that it is important to limit the lens entrance angle, and the energy spread, if possible, and to accelerate the beam to high energies prior to focusing with the lens. Unfortunately, very few data are available for chromatic aberration coefficients of electrostatic lenses. However, analytical expressions for upper limits for the chromatic aberrations of einzel and immersion lenses have been derived by El Kareh and El Kareh.[24]

The upper limit for the growth in size due to energy spread ΔE in an ion beam passing through an einzel lens operated in the acceleration-deceleration entrance-exit mode, referred to at the image plane, is given by

$$\Delta r_i \leq 2M\frac{\Delta E r_m}{E^{1/4}\phi_m^{3/4}} , \tag{18}$$

where ΔE is the energy spread in the ion beam of energy E, M is the magnification, ϕ_m is the variable potential

difference impressed on the einzel lens, and r_m is the radius of the beam as it passes through the lens. These formulas are expected to overestimate chromatic aberrational effects by the einzel lens.

3. Magnet aberrations

The 90° double-focusing magnet used in these studies will increase the phase space of the ion beam principally through second-order and energy dispersion effects. Chromatic aberrations due to the magnet are found to be negligibly small.

4. Second-order aberration

For equal object and image distances, the image of a point source passing through the 90° magnet will be increased in half width in the plane of dispersion (x direction) by[26]

$$\Delta x_i \simeq \frac{\rho}{2}\theta_{ix}^2 , \tag{19}$$

where ρ is the radius of the central orbit of the ion beam and θ_{ix} is the half angle of the beam entering or exiting the magnet.

5. Chromatic aberration

The image in the plane of dispersion of the magnet utilized in these investigations will be increased due to energy spread ΔE in the beam of energy E by amounts[26]

$$\Delta x_i = \frac{3}{4} x_1 \frac{\Delta E}{E} \tag{20}$$

and

$$\Delta y_i = y_1 \frac{\Delta E}{E} \tag{21}$$

where the x and y directions, respectively, and where x_1 and y_1 are the half widths of the beam at the object point of the magnet.

6. Dispersive effects due to energy spread

For particles of the same mass but different energies, the image half width Δx_i in the plane of dispersion (x direction) attributable to an energy spread ΔE is given by[27]

$$\Delta x_i = \frac{D}{4}\frac{\Delta E}{E} \tag{22}$$

where E_1 is the energy of the ion beams and D is the dispersion of the magnet given by

$$D = 4\rho$$

so that

$$\Delta x_i = \rho \frac{\Delta E}{E} . \tag{23}$$

7. Space charge effects

As a result of space charge, an ion beam of current I, diameter D, and energy E traveling a distance z will grow in size by an amount Δr given by[28]

$$\Delta r = r_0 \left\{ \cosh \left[2 \left[\frac{2e}{M} \right]^{-1/4} I^{1/2} \left[\frac{E}{e} \right]^{-3/4} \frac{z}{D} \right] - 1 \right\} , \tag{24}$$

where r_0 is the original size of the beam at $z=0$. From this expression, we again see the merit of accelerating beams to high energies. If we calculate the change in beam size within the source for an average energy of 1 keV for each of the negative-ion beams, we find that the beam changes by a negligibly small amount for each of the species. In fact, the negative-ion beam space charge within the source will be, most likely, more than compensated for by the counter-current cesium-ion beam. We, therefore, neglect this effect.

Many measurements have been made in attempts to delineate possible contributions to the emittances of the respective ion beams through space charge effects by varying the beam intensity, typically between 20 and 60 μA, from the source. In these measurements, the beam intensity was changed by changing the sputter probe voltage. In some cases, the emittances were found to increase slightly ($\sim 5\%$) with beam intensity, while for others, no increases were observed. We have also made estimates of the energy spreads due to space charge within the respective negative-ion beams by solving Poisson's equation for negative-ion flow within the source. In these calculations, we neglect the space charge compensating effects attributable to the counter-current flowing cesium-ion beam. Under this assumption, the energy spread due to space charge effects for the respective negative-ion beams would be

$^{28}Si^-$: $\Delta E \cong 5.6$ eV ;

$^{58}Ni^-$: $\Delta E \cong 2.04$ eV ;

$^{197}Au^-$: $\Delta E \cong 11.9$ eV

for an average energy of 1 keV. If we assume space charge compensation within the source, but none outside the source, these values are reduced by a factor of ~ 3.2.

VI. EMITTANCE AND ENERGY SPREAD ESTIMATIONS

The ion beam will grow in size after extraction from the source due to a combination of spherical and chromatic aberrations by the lens and due to second order, chromatic and energy dispersion by the magnet. We will assume that contributions to emittance growth due to different effects in a given element (lens or magnet) add in quadrature and that contributions to emittance growth in different elements add linearly. The emittances of an ion beam, after having passed through the einzel lens and momentum analysis system, at the focal plane of the momentum analysis system, can then be expressed in analytic form through the following relationships:

$$\epsilon_x \cong |M_x(Mx_0+\Delta x_1+\Delta x_2)\theta_{ix} \tag{25}$$

and

$$\epsilon_y \cong |M_y|(My_0+\Delta y_1+\Delta y_2)\theta_{iy} , \tag{26}$$

where

$$\Delta x_1 = \left[(MC_{so}\theta_{0x}^3)^2+\left[2M\frac{\Delta E}{E^{1/4}}\frac{r_m}{\phi_m^{3/4}}\right]^2\right]^{1/2},$$

$$\Delta x_2 = \left[\left[\frac{\rho\theta_{ix}}{2}\right]^2+\left[\rho\frac{\Delta E}{E}\right]^2+\left[\frac{3}{4}x_1\frac{\Delta E}{E}\right]^2\right]^{1/2},$$

$$\Delta y_1 = \left[(MC_{so}\theta_{0y}^3)^2+\left[2M\frac{\Delta E}{E^{1/4}}\frac{r_m}{\phi_m^{3/4}}\right]^2\right]^{1/2},$$

and

$$\Delta y_2 = y_1\frac{\Delta E}{E} .$$

Chromatic aberration of the beam by the magnet is negligibly small. Spherical aberration by the einzel lens dominates Δx_1 and Δy_1, while energy dispersion dominates Δx_2 and, in fact, is the largest contributor to emittance growth of the ion beam. These terms usually can be estimated rather accurately. Of the terms in Eqs. (25) and (26), the chromatic aberration expressions are the least accurate. Fortunately, they are not dominant, thus lending more credence to the following analytical approximations. In Eqs. (25) and (26), M_x and M_y are the magnification of the magnet in the x and y directions, respectively. For the magnet used in this work, $|M_x| \cong |M_y| \cong 1$.

As noted, beam growth due to aberrational effects induced by the einzel lens and momentum analysis system is greater in the x direction than in the y direction, principally due to second-order and energy-dispersive effects—effects that lead to the observed asymmetries in the emittances for the x and y directions for a particular ion species. Equations (25) and (26) provide important bases for making direct correlations between measured emittances ϵ and the energy spreads ΔE within ion beams, the origin of which can be traced to the intrinsic energy distribution within the negative-ion sputter generation process.

Ratios of the analytical approximations for the emittances given by Eqs. (25) and (26) offer a convenient means for comparing calculated and experimental results. We thus define

$$R_{x/y} = \frac{(\epsilon_{nx})_i}{(\epsilon_{ny})_i} = \frac{\{M_x(Mx_0+\Delta x_1+\Delta x_2)\theta_{ix}\sqrt{E}\}_i}{\{M_y(My_0+\Delta y_1+\Delta y_2)\theta_{iy}\sqrt{E}\}_i} \tag{27}$$

for $i=1,2,3$

and

$$R_{x/x} = \frac{(\epsilon_{nx})_j}{(\epsilon_{nx})_i} = \frac{\{M_x(Mx_0+\Delta x_1+\Delta x_2)\theta_{ix}\sqrt{E_1}\}_j}{\{M_x(Mx_0+\Delta x_1+\Delta x_2)\theta_{ix}\sqrt{E_1}\}_i}, \tag{28}$$

$$R_{y/y} = \frac{(\epsilon_{ny})_j}{(\epsilon_{ny})_i} = \frac{\{M_y(My_0+\Delta y_1+\Delta y_2)\theta_{iy}\sqrt{E}\}_j}{\{M_y(My_0+\Delta y_1+\Delta y_2)\theta_{iy}\sqrt{E}\}_i} , \tag{29}$$

$$R_{xy/xy} = \frac{(\epsilon_{nxy})_j}{(\epsilon_{nxy})_i} = \frac{(\sqrt{\epsilon_{nx}\epsilon_{ny}})_j}{(\sqrt{\epsilon_{nx}\epsilon_{ny}})_i} , \tag{30}$$

for $j=1, 2, 3$, and $i=1$.

The following designations are used for the respective species in Eqs. (27)–(30): $^{28}Si^- = 1$, $^{58}Ni^- = 2$, and $^{197}Au^- = 3$.

VII. RESULTS

Figures 3 and 4 show normalized x- and y-direction emittance contours versus percentage momentum analyzed ion beam intensity for $^{28}Si^-$, Figs. 5 and 6 for $^{58}Ni^-$, and Figs. 7 and 8 for $^{197}Au^-$. These data are typical of the 10 sets of data accumulated for each of the three negative-ion species.

The emittances and brightnesses per unit beam intensity versus percentage momentum analyzed ion beam intensity for $^{28}Si^-$, $^{58}Ni^-$, and $^{197}Au^-$ extracted from the source under identical operating conditions are shown in Figs. 9 and 10. In Fig. 10, the brightnesses of the respective ion beams have been divided by the ion beam intensity in order to illustrate further species-dependent effects. These data are derived from 10 or more measurements with standard deviations typically ranging from 3% to 6%. The results of these measurements clearly exhibit a previously unseen species-dependent effect.

Since the 90° double-focusing magnet contributes to the emittance growth in the x direction through second-order and energy-dispersion effects, the x-direction con-

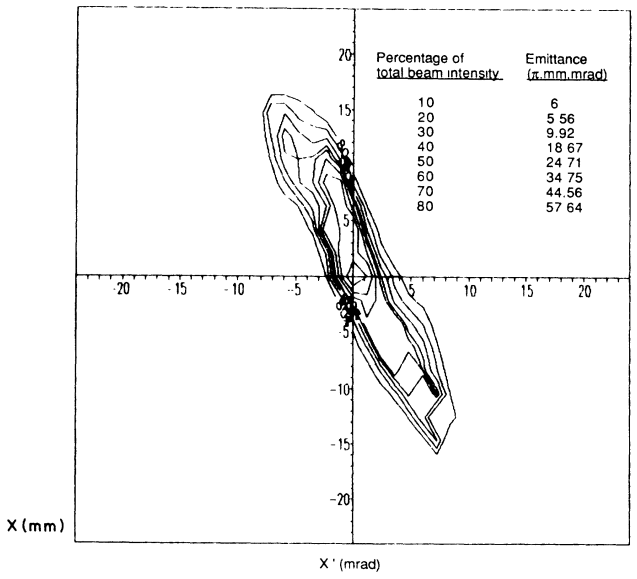

FIG. 3. x-direction emittance contours for $^{28}Si^-$ extracted from the ellipsoidal geometry ionizer negative-ion source: ion beam intensity: 60 μA; ion beam energy 20 keV.

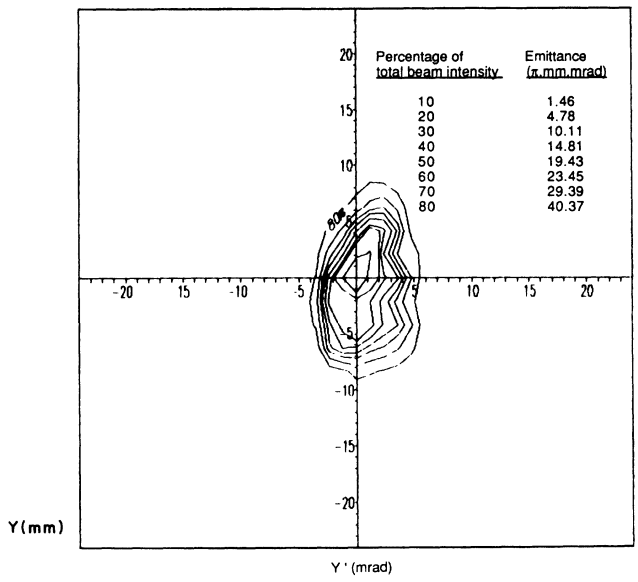

FIG. 4. y-direction emittance contours for $^{28}Si^-$ extracted from the ellipsoidal geometry ionizer negative-ion source: ion beam intensity: 60 μA; ion beam energy 20 keV.

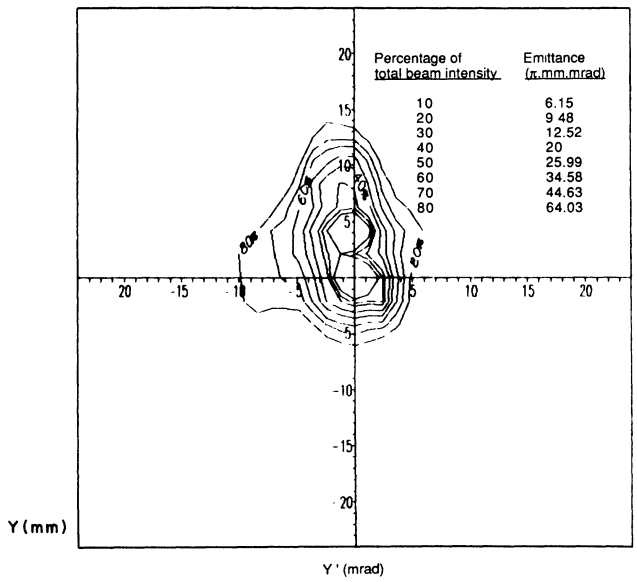

FIG. 6. y-direction emittance contours for $^{58}Ni^-$ extracted from the ellipsoidal geometry ionizer negative-ion source: ion beam intensity: 13 μA; ion beam energy 20 keV.

tours will be, in general, larger than their y-direction counterparts. This effect can be most easily seen by analysis of the data in terms of the ratios of the average of all x-direction 80% emittance contour data to those for the y direction for each of the three species.

By substitution of actual or estimated parameters for the einzel lens, magnet, ion beam, and optical arrangement of the facility (Fig. 2), e.g., C_{so}, M_x, M_y, θ_0, ϕ_m, r_m, E, ρ, x_0, y_0, θ_{ix}, and θ_{iy} into Eq. (27) and letting the unknown ΔE be the dependent variable in the expression, we arrive at the relationship between $R_{x/y}$ and ΔE shown in Fig. 11. The theoretically derived ratios $R_{x/y}$ of x to y emittances versus energy spread ΔE for each of the three species are found to lie on a common curve, thus providing a universal curve for correlating emittance and the energy spread ΔE within an ion beam. From Fig. 11, the

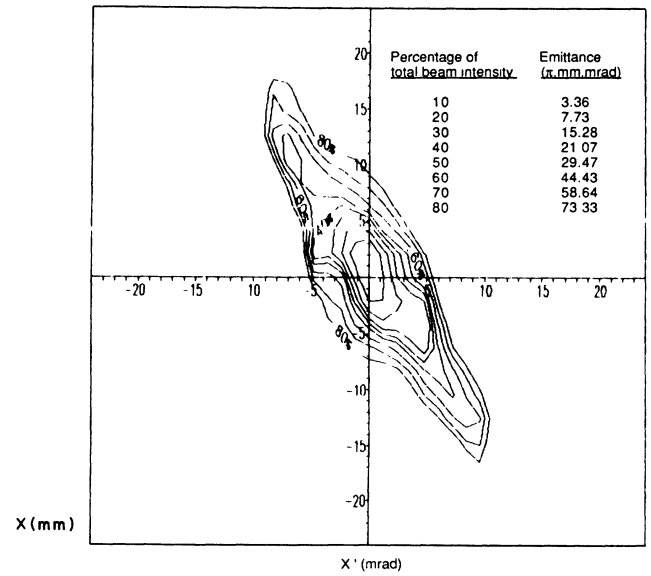

FIG. 5. x-direction emittance contours for $^{58}Ni^-$ extracted from the ellipsoidal geometry ionizer negative-ion source: ion beam intensity: 13 μA; ion beam energy 20 keV.

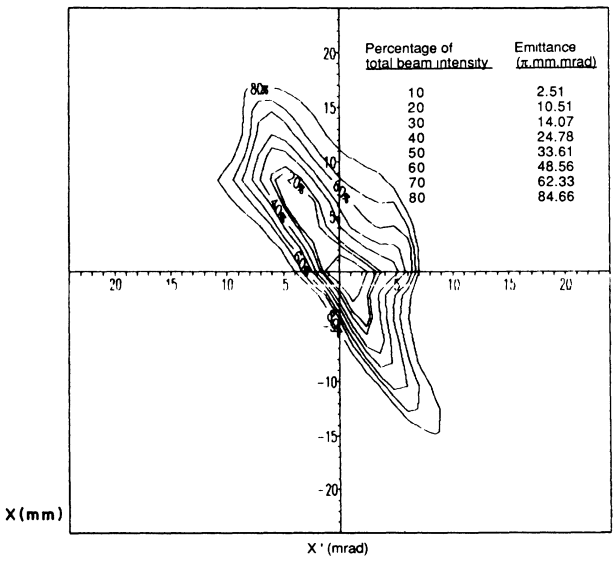

FIG. 7. x-direction emittance contours for $^{197}Au^-$ extracted from the ellipsoidal geometry ionizer negative-ion source: ion beam intensity: 26 μA; ion beam energy 20 keV.

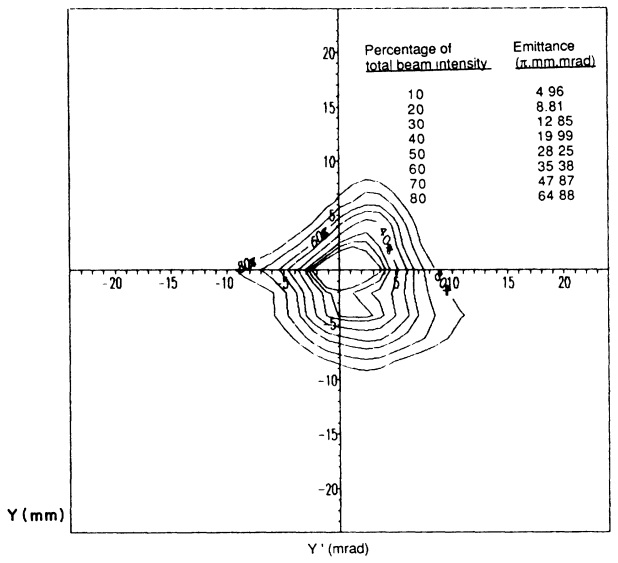

FIG. 8. y-direction emittance contours for $^{197}Au^-$ extracted from the ellipsoidal geometry ionizer negative-ion source: ion beam intensity: 26 μA; ion beam energy 20 keV.

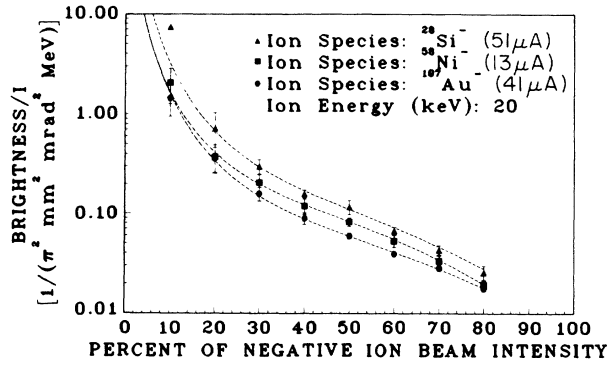

FIG. 10. Normalized brightness per unit ion beam intensity, B, versus percentage ion beam intensity for $^{28}Si^-$, $^{58}Ni^-$, and $^{197}Au^-$ illustrating a species-dependent effect. The error bars represent standard deviations in the emittance measurement for a given contour.

estimated energy spreads for the three species are found to be

$$^{28}Si^-: \ \Delta E(\text{eV})=22.7 \ ,$$

$$^{58}Ni^-: \ \Delta E(\text{eV})=31.3 \ ,$$

$$^{197}Au^-: \ \Delta E(\text{eV})=45.5 \ .$$

These estimations are seen to be realistic in magnitude, but appreciably higher than the results of Doucas[17] who measured the energy distributions of $^{12}C^-$, $^{32}S^-$, and $^{127}I^-$ extracted from a Middleton-type cone geometry negative-ion source at $E_1 \simeq 20$ keV.[29] The full width half maxima (FWHM) for $^{12}C^-$ ion beams were typically found to be $\Delta E \simeq 10$ eV with a base width of ~ 30 eV. However, this particular ion source and ion extraction geometry discriminates against high-energy secondary ions generated in the sputtering process,[30] unlike the source utilized in these experiments. Therefore, we anticipate somewhat larger energy spreads in the ion beams associated with the present measurements.

As a further test of the validity of Eqs. (27)–(30), we compared the measured emittance ratios $R_{x/y}$, $R_{x/x}$, $R_{y/y}$, and $R_{xy/xy}$ with their theoretically derived counterparts. Calculated and measured $R_{x/y}$, $R_{x/x}$, $R_{y/y}$, and $R_{xy/xy}$ values are seen to be in almost precise agreement and thus provide an explanation of the asymmetries observed between the x- and y-direction emittances of momentum analyzed ion beams. The origin of the increase in the x-direction emittance over the y-direction counterpart is because of the energy dispersive effects of the magnetic analysis system due to the intrinsic energy spread within a particular ion beam. There are physical

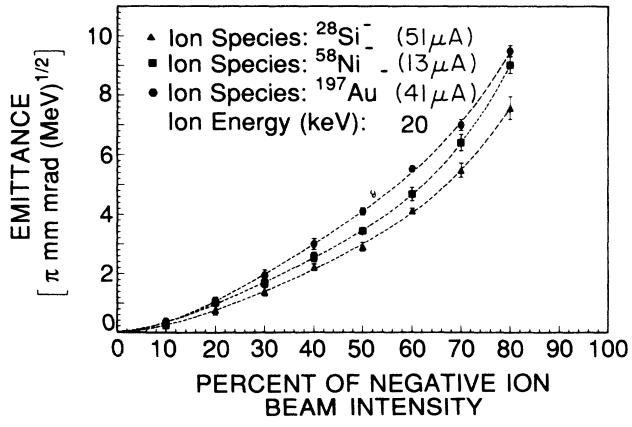

FIG. 9. Normalized emittance, ϵ_n vs percentage ion beam intensity for $^{28}Si^-$, $^{58}Ni^-$, and $^{197}Au^-$ illustrating a species-dependent effect. The error bars represent standard deviations in the emittance measurement for a given contour.

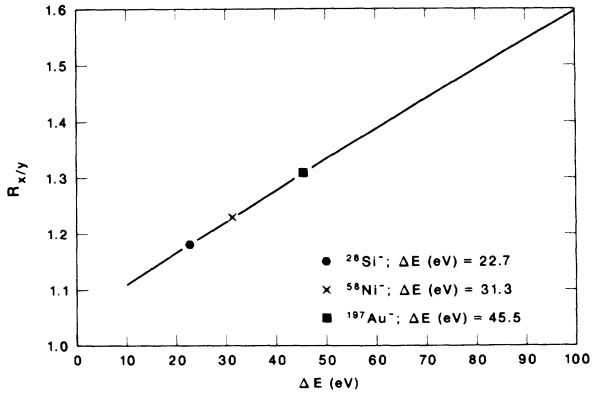

FIG. 11. Calculated ratios $R_{x/y}$ of x-direction to y-direction emittances vs energy spread ΔE.

reasons why we should expect differences in energy spread between negative-ion species sputter generated by a common projectile at the same energy. First of all, the maximum energy transfer between the projectile and different target atoms is different, as evidenced by E' in Eq. (4). Secondly, assuming the validity of the Nørskov and Lundqvist[6] model for negative ion formation, the energy distributions of sputter-generated negative ions are sensitive to the work function of the surface which varies with adsorbate coverage and thus the energy spreads from different species are expected to vary from this effect, as well.

VIII. CONCLUSIONS

We have developed high-resolution emittance measurement techniques which, when applied to the study of sputter-generated $^{28}Si^-$, $^{58}Ni^-$, and $^{197}Au^-$ negative-ion beams, has delineated a previously unseen species-dependent effect in the emittance of these beams; the origin of the effect is believed to be principally attributable to differences in the intrinsic energy distribution associated with the respective sputter generation process.

The energy spreads ΔE, estimated from these investigations, are larger than those previously measured by Doucas[17] (FWHM for $^{12}C^-$: $\Delta E \simeq 10$ eV) from a Middleton-type cone-geometry source;[29] however, this source extraction geometry discriminates against high-energy particles ejected during the sputter process.[30] The energy spreads of the negative-ion species are expected to be larger than their neutral particle parent atoms if the mechanism of ion formation is dependent on the ejection velocity of the particle; according to this model, the probability for ion formation favors the higher velocity components of the neutral particle energy distribution as seen from Eq. (2). For example, the average energies $\bar{E}$ of neutral particles sputtered from Si, Ni, and Au samples with a 1.2-keV krypton ion beam are found to be as follows: Si, $\bar{E} \simeq 10$ eV; Ni, $\bar{E} \simeq 18$ eV; Au, $\bar{E} \simeq 21$ eV,[18] while those from Cu, Nb, and V under bombardment with a 2-keV Ar ion beam are found to have the following values: Cu, $\bar{E} \cong 11.1$ eV; Nb, $\bar{E} \cong 16$ eV; V, $\bar{E} \cong 15.4$ eV.[14] The energy spreads derived from the emittance data of these investigations are considerably higher than the typical average energies of neutral sputtered particles and, thus these results are commensurate with a velocity-dependent negative-ion formation mechanism such as proposed by Nørskov and Lundqvist.[6]

These investigations show a previously unseen emittance dependence on negative-ion species, the origin of which is principally attributable to differences in the intrinsic energy distributions associated with the sputter-generation process. The energy spreads required to explain the asymmetries between the x and y emittance directions for the respective beams are too large to be explained by space-charge effects. Thus, the results of these investigations reflect on the fundamental processes which occur during negative-ion ejection (e.g., differences in momentum transfer, surface work function $\phi(\sigma)$, surface binding energy E_b, and image potential V_i). Through these measurements, we not only show how emittances of momentum analyzed ion beams are affected by the intrinsic energy spreads within the particular ion beam, but as well demonstrate how high-resolution emittance measurements can be used to obtain formation concerning energy spreads within a particular ion beam.

ACKNOWLEDGMENTS

The authors express their application to Dr. C. M. Jones for constructive criticism of the manuscript. Research sponsored by the U.S. Department of Energy Under Contract No. DE-AC05-84OR21400 with Martin Marietta Energy Systems, Inc.

[1]R. Middleton, Nucl. Instrum. Methods **214**, 139 (1983).
[2]G. D. Alton, Nucl. Instrum. Methods A **244**, 133 (1986).
[3]G. D. Alton and G. D. Mills, IEEE Trans. Nucl. Sci. **NS-32**, 1822 (1985).
[4]A. Blandin, A. Nourtier, and D. W. Hone, J. Phys. (Paris) **37**, 369 (1976).
[5]M. L. Yu, Phys. Lett. **40**, 574 (1978).
[6]J. K. Nørskov and B. I. Lundqvist, Phys. Rev. B **19**, 5661 (1979).
[7]G. D. Alton, Proceedings of the Third International Conference on Electrostatic Accelerator Technology, Oak Ridge, 1981 (unpublished), p. 228.
[8]Z. Sroubek, Phys. Rev. B **25**, 6046 (1982).
[9]G. Blaise and A. Nourtier, Surf. Sci. **90**, 495 (1979).
[10]P. Williams, Surf. Sci. **90**, 588 (1979).
[11]K. Wittmaack, in *Inelastic Ion-Surface Collisions*, edited by N. Tolk, J. C. Tully, W. Heiland, and C. W. White (Academic, New York, 1977).
[12]M. J. Vasile, Phys. Rev. B **29**, 3785 (1984).
[13]M. L. Yu, Phys. Rev. Lett. **47**, 1325 (1981).
[14]J. Dembowski, H. Oeschsner, Y. Yamamura, and M. Urbassek, Nucl. Instrum. Methods B **18**, 464 (1987).
[15]P. Sigmund, in *Inelastic Ion Surface Collisions*, edited by H. Tolk, J. C. Tully, W. Heiland, and C. W. White (Academic, New York, 1977), p. 121.
[16]M. W. Thompson, Philos. Mag. **18**, 377 (1968).
[17]G. Doucas, Int. J. Mass Spec. Ion Phys. **25**, 71 (1977).
[18]G. K. Wehner and G. S. Anderson, in *Handbook of Thin Film Technology*, edited by L. I. Maissel and R. Glang (McGraw-Hill, New York, 1970), Chap. 3.
[19]G. D. Alton, J. W. McConnell, S. Tajima, and G. J. Nelson, Nucl. Instrum. Methods B **24/25**, 826 (1987).
[20]G. D. Alton and J. W. McConnell, Nucl. Instrum. Methods A **268**, 445 (1988).
[21]T. R. Walsh, J. Nucl. Eng., Part C **4**, 53 (1962).
[22]G. D. Alton, Proceedings of the Eleventh Symposium on Ion Sources and Ion-Assisted Technology, 1987 (unpublished), p. 157.
[23]G. D. Alton, Surf. Sci. **175**, 226 (1986).
[24]A. B. El Kareh and J. C. J. El Kareh, *Electron Beams, Lenses, and Optics* (Academic, New York, 1970), Vol. 2.
[25]G. Liebmann, Proc. Phys. Soc. **62**, 15 (1949).
[26]J. J. Livingood, *The Optics of Dipole Magnets* (Academic, New York, 1969), Chap. 17.

[27]J. J. Livingood, *The Optics of Dipole Magnets* (Academic, New York, 1969), Chaps. 2 and 4.
[28]V. K. Zworykin, G. A. Morton, E. G. Ramberg, J. Hiller, and A. W. Vance, *Electron Optics and the Electron Microscope* (Wiley, New York, 1945), Chap. 16.
[29]R. Middleton and C. T. Adams, Nucl. Instrum. Methods **122**, 35 (1974).
[30]G. D. Alton, Rev. Sci. Instrum. **59**, 1045 (1988).

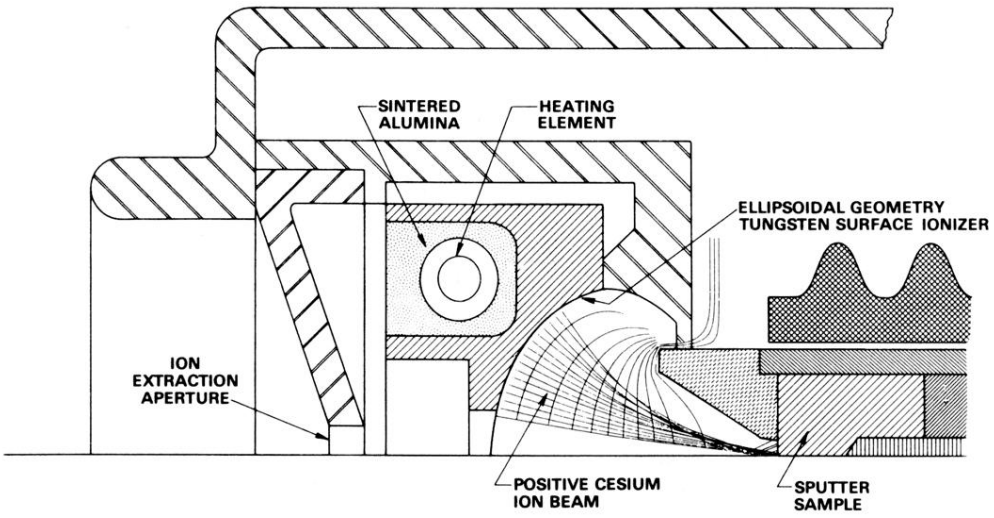

FIG. 1. Schematic drawing of the ellipsoidal geometry ionizer negative-ion source showing computer simulated cesium-ion trajectories in the ionizer-sputter probe region of the source.